Acta Crystallographica Section A
Foundations of Crystallography
ISSN 0108-7673

Received 24 February 2003
Accepted 22 April 2003

'Six-beam X-ray section topograph' images and computer-simulated images using the new *n*-beam dynamical theory based on the Takagi–Taupin equations

Kouhei Okitsu,[a]* Yasuhiko Imai,[b] Yoshinori Ueji[c] and Yoshitaka Yoda[b]

[a]Engineering Research Institute, School of Engineering, The University of Tokyo, Yayoi, Bunkyo-ku, Tokyo 113-8656, Japan, [b]Japan Synchrotron Radiation Research Institute, 1-1-1 Kouto, Mikazuki-cho, Sayo-gun, Hyogo 679-5198, Japan, and [c]Graduate School of Frontier Sciences, The University of Tokyo, 5-1-5 Kashiwanoha, Kashiwa-shi, Chiba 277-8562, Japan. Correspondence e-mail: okitsu@soyak.t.u-tokyo.ac.jp

A 'six-beam X-ray section topograph' experiment was performed whose images are in excellent agreement with the images computer-simulated using the theory derived by one of the authors [Okitsu (2003). *Acta Cryst.* A**59**, 235–244] based on the Takagi–Taupin dynamical theory. X-rays whose wavefront was limited to 0.1×0.1 mm were incident on a $[1\bar{1}1]$-oriented floating-zone silicon crystal with thickness of 9.911 mm so that a six-beam condition was satisfied. The six reflection indices were 000 (forward diffraction), 440, 484, 088, $\bar{4}48$ and $\bar{4}04$. The plane of incidence of the 088 reflection was adjusted so as to be perpendicular to the direction of the incident horizontal linear polarization of the synchrotron radiation, which was monochromated into 18.5 keV (0.670 Å wavelength). While the simulations were performed under the assumptions that the incident X-rays were linearly polarized both horizontally and vertically, they were evidently different and only the simulated images under the assumption of horizontally polarized incident X-rays were in excellent agreement with the images obtained by the experiment.

1. Introduction

The possibility that the structure-factor phase information can be extracted from the analysis of three-beam X-ray diffraction profiles was pointed out by Ott (1938), Bijvoet & MacGillavry (1939) and Lipscomb (1949). Since the experimental work was published by Colella (1974), analysis of X-ray three-beam diffraction has come to be recognized as one of the most effective methods to solve the phase problem in crystal structure analysis (Post, 1977, 1979; Shen, 1986; Chang, 1986; Weckert *et al.*, 1993; Weckert & Hümmer, 1997, 1998; Thorkildsen & Larsen, 1998; Larsen & Thorkildsen, 1998; Stetsko *et al.*, 2001).

Incidentally, Kato (1976*a*,*b*, 1979, 1980*a*,*b*) derived the statistical dynamical theory to deal with the behavior of X-rays in a mosaic crystal based on the Takagi–Taupin equations (Takagi, 1962, 1969; Taupin, 1964). Thorkildsen (1987), Thorkildsen & Larsen (1998), Larsen & Thorkildsen (1998) and Thorkildsen *et al.* (2001) pointed out that a theory could be derived that can deal with the behavior of X-rays in a three-beam diffraction case in a mosaic crystal whose structure is to be solved if Kato's procedure were applied to a Takagi–Taupin type dynamical theory extended to the three-beam case. Thorkildsen (1987) attempted to extend the Takagi–Taupin equations to the three-beam case. However, the extended theory neglects the effect of polarization. Okitsu (2003) has recently derived a Takagi–Taupin-type dynamical theory extended to *n*-beam ($n \in \{3, 4, 6, 8, 12\}$) cases that can deal with the effect of polarization correctly. Furthermore, a method to solve the theory numerically was also given by Okitsu (2003). The aim of the present paper is to verify the new theory by comparing the experimental result and the result computer-simulated based on the new theory.

The first computer-simulated section topograph image compared with an experimental section topograph image of a dislocation in a crystal was presented by Balibar & Authier (1967), based on an algorithm that can numerically integrate the Takagi–Taupin equations (Authier *et al.*, 1968). These works were followed by studies on computer-simulated images of dislocations (Epelboin, 1974; Chukhovskii, 1974), planar defects (Epelboin, 1979), ferromagnetic domain walls (Nourtier *et al.*, 1979) and strain centers (Green *et al.*, 1990; Okitsu *et al.*, 1992) on section topographs in the Laue geometry, and studies on computer-simulated dislocation images (Bedynska, 1973; Bedynska *et al.*, 1976; Bubáková & Šourek, 1976; Gronkowski, 1980; Riglet *et al.*, 1980) on topographs in the Bragg geometry. In the above works, algorithms with a constant integration step length (constant step algorithm)

were used. On the other hand, Epelboin (1983) developed an algorithm in which calculation step length was varied (varying step algorithm). In the varying step algorithm, the calculation step can be automatically changed so that the step length is small where the phase of the X-ray wave changes rapidly in the crystal. The circumstances related to the computer simulation using the Takagi–Taupin equations were reviewed by Epelboin (1985, 1987).

Recently, Heyroth *et al.* (2001) simulated three-beam pinhole topograph images based on an Ewald–Laue-type three-beam theory and compared them with experimental results performed at ESRF (Heyroth *et al.*, 1999). On the other hand, in the present work, the simulations comparable with the experimental results obtained at SPring-8 were performed using the new Takagi–Taupin-type *n*-beam dynamical theory one of the present authors has derived (Okitsu, 2003).

2. Experimental

Fig. 1 shows the experimental arrangement of 'six-beam X-ray section topography'. The first-order undulator radiation from BL09XU of SPring-8 was monochromated into 18.5 keV with silicon monochromator crystals which gave two consecutive 111 reflections. The degree of horizontal polarization of the monochromated X-rays had been estimated to be 0.994. X-rays whose dimension was limited to 1 × 1 mm by a four-quadrant slit system were incident on a [1$\bar{1}$1]-oriented floating-zone silicon crystal whose surfaces were mechanically and chemically polished. The thickness of the crystal was 9.911 mm. The crystal was mounted on a θ–ω–φ three-axis goniometer so that θ, ω and φ axes were parallel to [21$\bar{1}$], [1$\bar{1}$1] and [011] directions of the crystal, respectively, as shown in Fig. 1. This situation in the reciprocal space is shown in Fig. 2. A two-axis swivel-type goniometer whose φ axis was mounted on the ω axis was equipped on a tangent-bar-type θ-axis goniometer. The θ axis was adjusted to be horizontal and perpendicular to the incident X-ray beam axis.

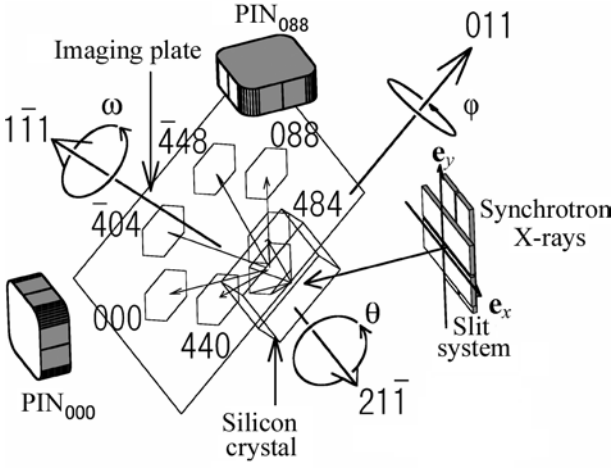

Figure 1
A schematic drawing of the 'six-beam X-ray section topography' experiment. The photon energy was 18.5 keV. The polarization of the incident X-rays was horizontal, that is the direction of $\mathbf{e}_x$.

First, the forward-diffracted and 088-reflected X-rays were monitored with PIN photodiodes PIN_{000} and PIN_{088} in Fig. 1 rotating the crystal around the θ axis. Two of the present authors (YI and YY) found that a 088 reflection peak was observed at the angular middle position of θ between two intensity peaks of forward-diffracted X-rays. The two peaks of forward-diffracted X-rays were assigned to anomalous transmission arising from 440 and $\bar{4}$04 reflections. The peaks split since the θ axis was not completely perpendicular to the [1$\bar{1}$1] direction of the crystal. Then, the φ axis was adjusted so that the intensity of the forward-diffracted beam did not split but gave a single peak at an angular position of θ, at which the peak of 088-reflected X-rays was observed simultaneously, which resulted in the satisfying of the six-beam case of 000, 440, 484, 088, $\bar{4}$48 and $\bar{4}$04 reflections. Some dynamical diffraction parameters related to these reflection indices are summarized in Table 1. Under the condition of the six-beam case, the dimension of the incident X-rays was further limited to 0.1 × 0.1 mm, when the 'six-beam X-ray section topograph' images were recorded.

3. Computer simulations

The method to solve the new theory numerically in the case of '*n*-beam X-ray section topography' is in a separate paper (Okitsu, 2003). The computer simulations were performed with the boundary conditions for the incidence of horizontally and vertically polarized X-rays. A crystal with thickness 9.911 mm was divided for calculation into 2000 layers of identical thickness in the [1$\bar{1}$1] direction of the crystal. Each layer was divided into small hexagonal pyramids as shown in Fig. 3. The electric displacement amplitudes of X-rays at the apex of the small pyramid were calculated step by step by

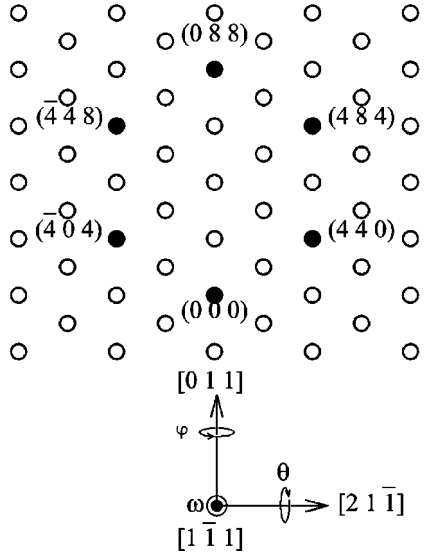

Figure 2
A schematic drawing in the reciprocal space corresponding to Fig. 1. The plane of the drawing is the cross section perpendicular to the [1$\bar{1}$1] direction. The reciprocal-lattice points that contribute to the present experiment are shown as solid circles.

Table 1
Parameters of X-ray reflection indices of silicon crystal: $|F_{\mathbf{h}}|$ is the absolute value of the crystal structure factor for the **h** reflection; $|\chi_{r\mathbf{h}}|$ and $|\chi_{i\mathbf{h}}|$ are the absolute values of the real and imaginary parts of $\chi_{\mathbf{h}}$, respectively, where $\chi_{\mathbf{h}}$ is the **h**th-order Fourier coefficient of electric susceptibility of the silicon crystal.

h	Bragg angle (°)	$\lvert F_{\mathbf{h}}\rvert$	$\lvert\chi_{r\mathbf{h}}\rvert$	$\lvert\chi_{i\mathbf{h}}\rvert$
000	0	112.5000	2.8292×10^{-6}	1.2600×10^{-8}
440	20.4270	48.8457	1.0854×10^{-6}	1.1134×10^{-8}
484	37.1935	25.6233	4.4453×10^{-7}	8.6938×10^{-9}
088	44.2689	20.7667	3.1832×10^{-7}	7.6823×10^{-9}
$\bar{4}48$	37.1935	25.6233	4.4453×10^{-7}	8.6938×10^{-9}
$\bar{4}04$	20.4270	48.8457	1.0854×10^{-6}	1.1134×10^{-8}

solving equation (40) in Okitsu (2003). Therefore, the calculation algorithm to integrate the new six-beam X-ray dynamical diffraction theory is a three-dimensional constant step algorithm. The calculation step length l_1 in Fig. 3 corresponding to the value of $\left|\overrightarrow{R_i^{(0)}R^{(1)}}\right|$ defined in Okitsu (2003) was 6.92 μm. The extinction length of the forward diffraction was calculated to be 23.7 μm. $\left|\overrightarrow{R_i^{(0)}R^{(1)}}\right|$ is small compared to this value.

4. Results and discussion

The 'six-beam X-ray section topograph' images were simultaneously recorded on an imaging plate set 27.3 mm behind the crystal so as to be parallel to the $(1\bar{1}1)$ surface of the crystal. The pixel size of the imaging plate was 50 × 50 μm. Fig. 4 shows the images taken with an exposure time of 30 s. In the center of Fig. 4, a horizontal bar corresponding to 10 mm is drawn. A dark gray level shows a high intensity of X-rays.

Fig. 5[$Xy(z)$] summarizes the results of experiment (expansions of Fig. 4) and the computer simulation, where X is E or S (experiment or simulation, respectively), y is h or v (with the incidence of horizontal or vertical polarization, respectively) and $z \in \{a, b, c, d, e, f\}$ corresponds to 000, 440, 484, 088, $\bar{4}48$ and $\bar{4}04$ reflections, respectively. Each calculation for obtaining $Sh(z)$ and $Sv(z)$ ($z \in \{a, b, c, d, e, f\}$) took three weeks of CPU time on a personal computer with a Pentium III 1 GHz processor. The original pixel size of all computer-simulated images shown hereafter is 13.37 × 13.37 μm.

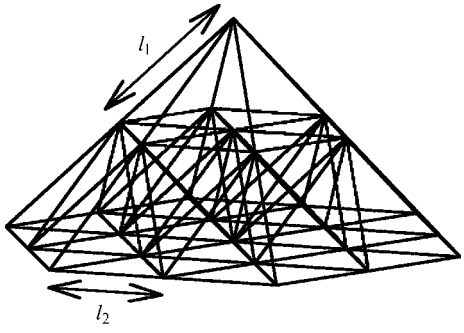

Figure 3
The crystal was divided into small hexagonal pyramids for simulation. The lengths l_1 and l_2 were assumed to be 6.92 and 4.83 μm.

Figs. 5[$Sh(z)$] and [$Eh(z)$] ($z \in \{a, b, c, d, e, f\}$) are in excellent agreement in detail whereas Figs. 5[$Sv(z)$] evidently differ from Figs. 5[$Eh(z)$], which reveals that the new theory and the computer program can correctly deal with the behavior of X-rays in the six-beam case taking into account the effect of polarization. The vertically striped patterns in the right-lower regions of Figs. 5[$Eh(z)$] ($z \in \{a, b, c, d, e, f\}$) are considered to be striations introduced when the crystal was grown. This shows that 'n-beam X-ray section topography' will be a useful tool to estimate minute strain fields in nearly perfect crystals when coupled with the simulation.

During the calculation procedure until the simulated results shown in Figs. 5[$Sh(z)$] ($z \in \{a, b, c, d, e, f\}$) are obtained, topograph images are simulated for a crystal with small thicknesses up to the thickness of the real crystal (9.911 mm). Figs. 6(a), (b), (c) and (d) show 'six-beam X-ray section topograph' images computer-simulated under the assumption that the thickness of the crystal is $p \times 9.911$ mm and the distance of the imaging-plate position from the crystal is $p \times 27.3$ mm, where the values of p are 0.25, 0.5, 0.75 and 1, respectively. The features of Figs. 6(a), (b), (c) and (d) are almost identical in contrast to *Pendellösung* fringes which appear on two-beam X-ray section topograph images. Figs. 7(a), (b), (c) and (d) show expansions of forward-diffracted X-ray images in Figs. 6(a), (b), (c) and (d). Figs. 8(a), (b), (c) and (d) show X-ray intensity profiles along the horizontal black lines in Figs. 7(a), (b), (c) and (d). Figs. 7 and 8 show more clearly that X-ray intensity distribution almost does not change with propagation in the crystal. X-ray intensity peaks indicated by white arrows in Fig. 7(d) and by black arrows in Fig. 8(d) are observed also in Figs. 7(a), (b), (c) and Figs. 8(a), (b), (c). Further, similar black spots can be observed also in Figs. 5[$Sh(z)$], where $z \in \{a, b, c, d, e, f\}$, which shows that X-ray energy flow has a maximum value in these positions in the crystal for any reason. It can be considered that the enhanced Borrmann effect plays an important role rather than the extinction effect in the six-beam case.

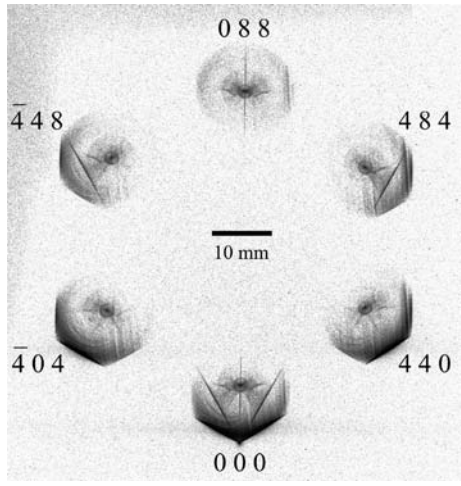

Figure 4
Images obtained by the 'six-beam X-ray section topograph' experiment.

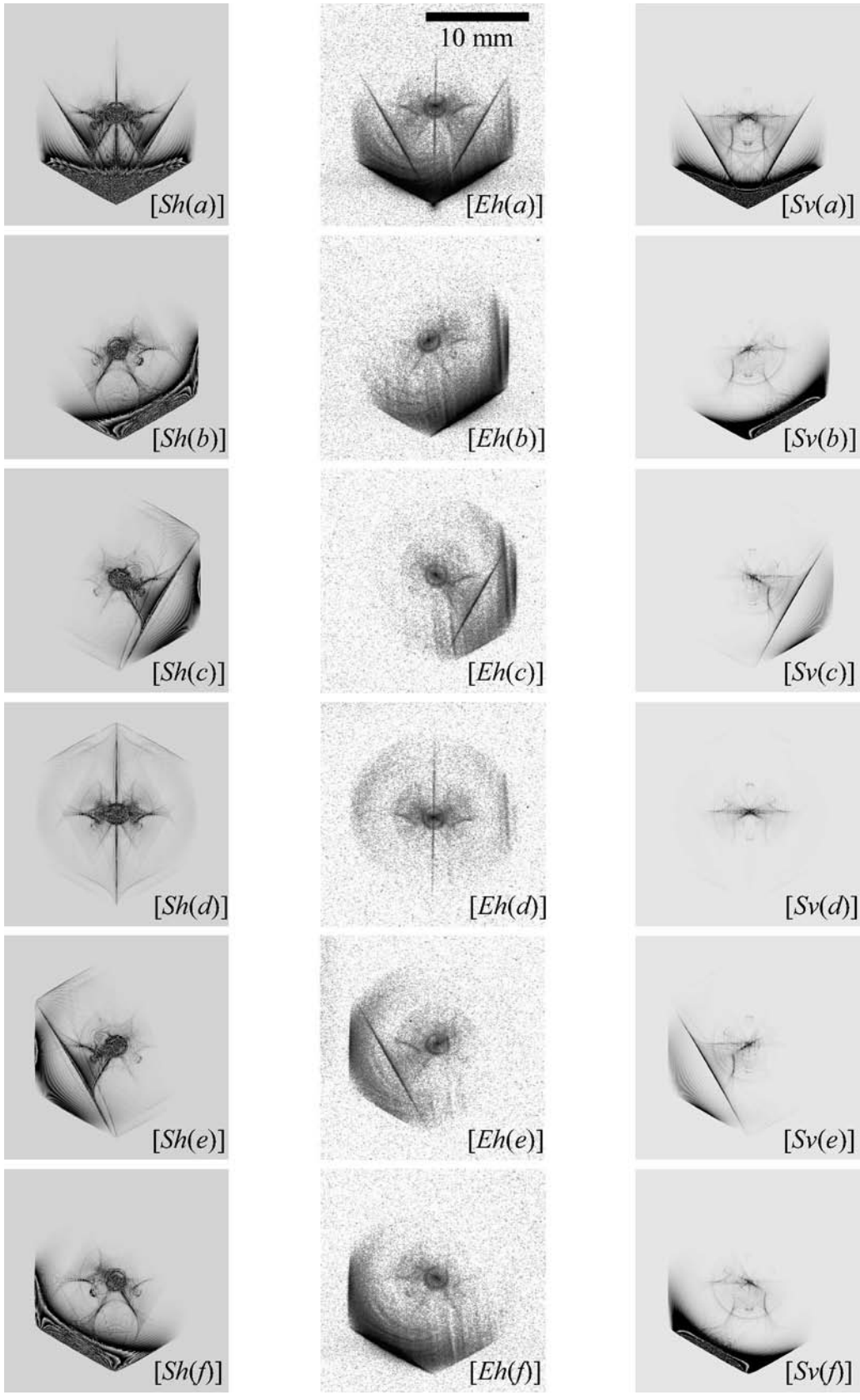

Figure 5
Experimental and computer-simulated images of the 'six-beam X-ray section topographs', the arrangement of which is shown in Fig. 1. [$Xy(z)$] means an image by X ($X \in \{S, E\}$, where S is the simulation and E is the experiment), with the y-polarized incident X-rays ($y \in \{h, v\}$, where h is horizontal and v is vertical) and for z reflection ($z \in \{a, b, c, d, e, f\}$, where a, b, c, d, e and f correspond to 000, 440, 484, 088, $\bar{4}48$ and $\bar{4}04$ reflections, respectively). A scale of 10 mm is drawn in the right-upper part of [$Eh(a)$] as a horizontal bar.

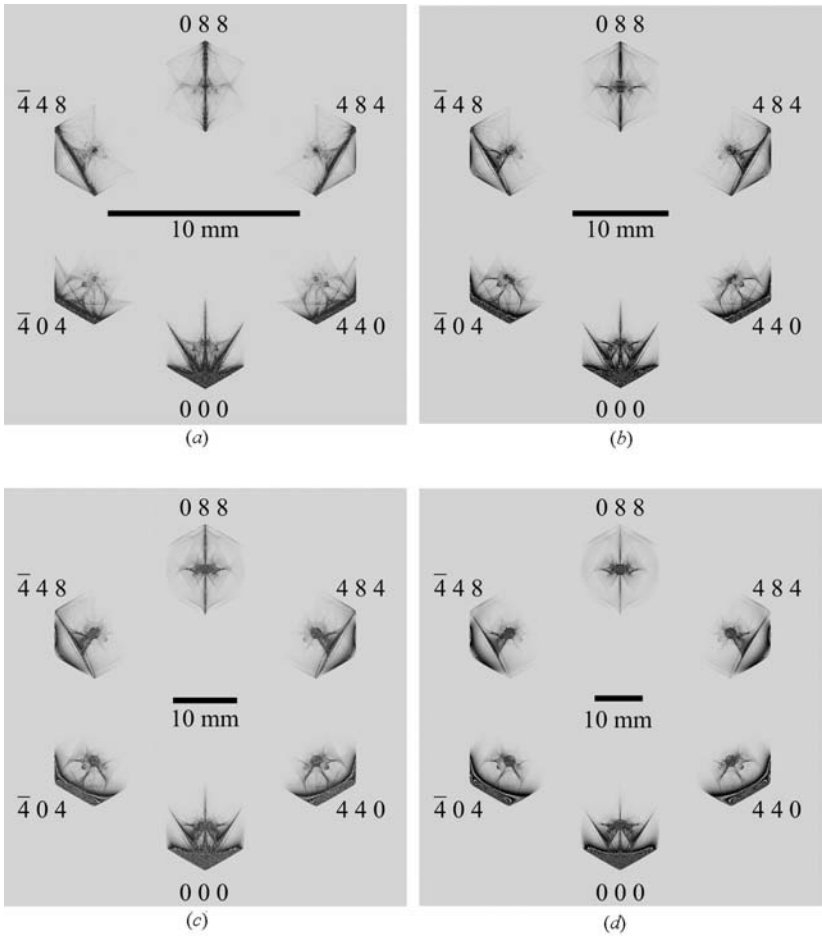

Figure 6
Computer-simulated results obtained by varying the thickness of the crystal and the imaging-plate position with the same ratio.

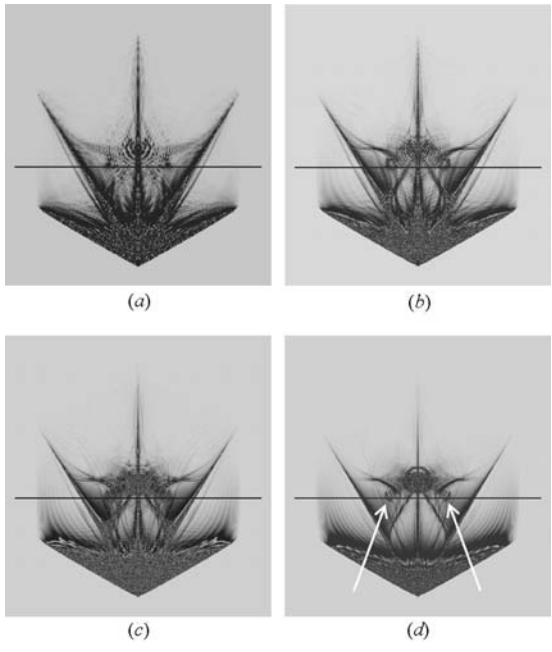

Figure 7
Magnification of forward-diffracted X-ray images in Fig. 6. The length of the horizontal black line is $p \times 2.0$ mm, where the values of p are 0.25, 0.5, 0.75 and 1 for (*a*), (*b*), (*c*) and (*d*), respectively.

5. Conclusions

The new theory (Okitsu, 2003) based on the Takagi–Taupin equations (Takagi, 1962, 1969; Taupin, 1964) and the computer program to solve the new theory have partly been verified for 'six-beam X-ray section topography' by comparing the experimental and the computer-simulated images. It was particularly revealed that the new theory can take into account the effect of polarization correctly. However, further studies to verify the new theory are necessary since the present work gives just one example of the agreement between the experiment and the computer simulation based on the new theory. The new theory will give the theoretical basis to develop X-ray optical devices applying the *n*-beam cases, for example a transmission-type monochromator (Kikuta, 2002), which takes advantage of the enhanced Borrmann effect.

The experimental part of the present work was performed with the approval of the Japan Synchrotron Radiation Research Institute (JASRI) (Proposal No. 2002 A0499-NMD3-np). The computer simulations of the present work were performed at the High-Power X-ray Laboratory, School of Engineering, The University of Tokyo. The present work is

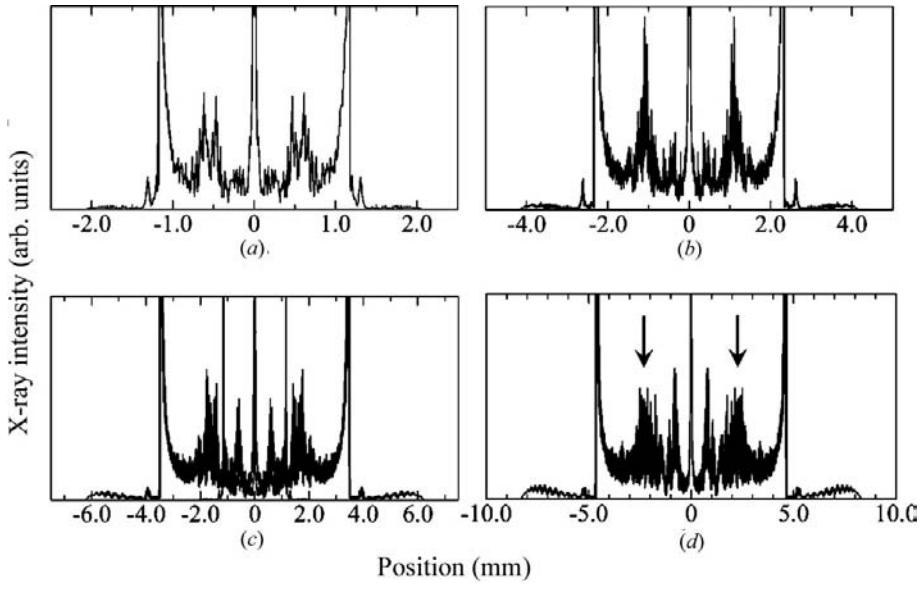

Figure 8
X-ray intensity profiles along horizontal lines in Fig. 7. (*a*), (*b*), (*c*) and (*d*) correspond to Figs. 7(*a*), (*b*), (*c*) and (*d*). The width of each graph is the same as each horizontal black line length in Fig. 7. The intensity peaks indicated by black vertical arrows in (*d*) correspond to point-like black spots indicated in Fig. 7(*d*).

one of the activities of the Active Nano-Characterization and Technology Project financially supported by Special Coordination Funds of the Ministry of Education, Culture, Sports, Science and Technology of the Japan Government. The authors are indebted to Professor Y. Amemiya of the School of Frontier Sciences, The University of Tokyo and Professor S. Kikuta of JASRI for their fruitful discussions and encouragement and also to Mr Y. Urano of the School of Frontier Sciences, The University of Tokyo, for his technical assistance in the present work.

References

Authier, A., Malgrange, C. & Tournarie, M. (1968). *Acta Cryst.* A**24**, 126–136.
Balibar, F. & Authier, A. (1967). *Phys. Status Solidi*, **21**, 413–422.
Bedynska, T. (1973). *Phys. Status Solidi A*, **18**, 147–154.
Bedynska, T., Bubáková, R. & Šourek, Z. (1976). *Phys. Status Solidi A*, **36**, 509–516.
Bijvoet, J. M. & MacGillavry, C. H. (1939). *Chem. Weekbl.* **36**, 330–331.
Bubáková, R. & Šourek, Z. (1976). *Czech. J. Phys. B*, **26**, 863–864.
Chang, S. L. (1986). *Phys. Rev. B*, **33**, 5848–5850.
Chukhovskii, F. N. (1974). *Kristallografiya*, **19**, 482–488.
Colella, R. (1974). *Acta Cryst.* A**30**, 413–423.
Epelboin, Y. (1974). *J. Appl. Cryst.* **7**, 372–377.
Epelboin, Y. (1979). *J. Appl. Phys.* **50**, 1312–1317.
Epelboin, Y. (1983). *Acta Cryst.* A**39**, 761–767.
Epelboin, Y. (1985). *Mater. Sci. Eng.* **73**, 1–43.
Epelboin, Y. (1987). *Prog. Cryst. Growth Charact.* **14**, 465–506.
Green, G. S., Fan, C.-S. & Tanner, B. K. (1990). *Philos. Mag. A*, **61**, 23–33.
Gronkowski, J. (1980). *Phys. Status Solidi A*, **57**, 105–112.
Heyroth, F., Höche, H.-R. & Eisenschmidt, C. (1999). *J. Phys. D: Appl. Phys.* **32**, A133–A138.
Heyroth, F., Zellner, J., Höche, H.-R., Eisenschmidt, C., Weckert, E. & Drakopoulous, M. (2001). *J. Phys. D: Appl. Phys.* **34**, A151–A157.
Kato, N. (1976*a*). *Acta Cryst.* A**32**, 453–457.
Kato, N. (1976*b*). *Acta Cryst.* A**32**, 458–466.
Kato, N. (1979). *Acta Cryst.* A**35**, 9–16.
Kato, N. (1980*a*). *Acta Cryst.* A**36**, 171–177.
Kato, N. (1980*b*). *Acta Cryst.* A**36**, 763–769.
Kikuta, S. (2002). Private communication.
Larsen, H. B. & Thorkildsen, G. (1998). *Acta Cryst.* A**54**, 137–145.
Lipscomb, W. N. (1949). *Acta Cryst.* **2**, 193–194.
Nourtier, C., Kleman, M., Taupin, D., Miltat, J., Labrune, M. & Epelboin, Y. (1979). *J. Appl. Phys.* **50**, 2143–2145.
Okitsu, K. (2003). *Acta Cryst.* A**59**, 235–244.
Okitsu, K., Iida, S., Sugita, Y., Takeno, H., Yagou, Y. & Kawata, H. (1992). *Jpn. J. Appl. Phys*, **31**, 3779–3785.
Ott, H. (1938). *Ann. Phys. (Leipzig) 5. Folge*, **31**, 264–288.
Post, B. (1977). *Phys. Rev. Lett.* **39**, 760–763.
Post, B. (1979). *Acta Cryst.* A**35**, 17–21.
Riglet, P., Sauvage, M., Pětroff, J. F. & Epelboin, Y. (1980). *Philos. Mag. A*, **42**, 339–358.
Shen, Q. (1986). *Acta Cryst.* A**42**, 525–533.
Stetsko, Y. P., Juretschke, H. J., Huang, Y.-S., Lee, Y.-R., Lin, T.-C. & Chang, S.-L. (2001). *Acta Cryst.* A**57**, 359–367.
Takagi, S. (1962). *Acta Cryst.* **15**, 1311–1312.
Takagi, S. (1969). *J. Phys. Soc. Jpn*, **26**, 1239–1253.
Taupin, D. (1964). *Bull. Soc. Fr. Minéral. Cristallogr.* **87**, 469–511.
Thorkildsen, G. (1987). *Acta Cryst.* A**43**, 361–369.
Thorkildsen, G. & Larsen, H. B. (1998). *Acta Cryst.* A**54**, 120–128.
Thorkildsen, G., Larsen, H. B. & Weckert, E. (2001). *Acta Cryst.* A**57**, 389–394.
Weckert, E. & Hümmer, K. (1997). *Acta Cryst.* A**53**, 108–143.
Weckert, E. & Hümmer, K. (1998). *Cryst. Res. Technol.* **33**, 653–678.
Weckert, E., Schwegle, W. & Hümmer, K. (1993). *Proc. R. Soc. London Ser. A*, **442**, 33–46.